Varactor-Tunable Second-Order Bandpass Frequency-Selective Surface With Embedded Bias Network

Amir Ebrahimi, *Student Member, IEEE*, Zhongxiang Shen, *Senior Member, IEEE*, Withawat Withayachumnankul, Said F. Al-Sarawi, *Member, IEEE*, and Derek Abbott, *Fellow, IEEE*

Abstract—A varactor-tunable second-order bandpass frequency-selective surface (FSS) for microwave frequencies is presented in this article. The FSS is composed of three stacked metallic layers. The wire grid in each layer in combination with metallic vias provides the bias for the varactors. This configuration eliminates the need for a dedicated bias network for the varactors, and thus avoids undesirable responses associated with the added bias grid. An equivalent circuit model together with an analytical design method is provided to simplify the design procedure of the FSS. The performance of the proposed structure is experimentally validated in a parallel-plate waveguide setup. Measurements show that by changing the varactor capacitance from 0.12 to 0.38 pF, the center frequency of the filter is tuned from 5.2 to 3.7 GHz with a consistent fractional bandwidth of 9% and with an insertion loss between 3 and 6 dB.

Index Terms—Electronic tuning, frequency-selective surfaces (FSSs), periodic structure, reconfigurable, varactor.

I. INTRODUCTION

FREQUENCY-SELECTIVE surfaces (FSSs) are two-dimensional (2-D) planar structures designed for manipulation of electromagnetic waves in different ways [1]. They have found many applications from the microwave up to the optical frequency ranges [2], [3]. For example, they can be used as spatial filters [4], [5] absorbers [6]–[8], lenses [9], [10], and reflectarrays [11], [12]. Nowadays, the vast demands and rapid developments in multifunctional and multistandard communication systems necessitate tunable and reconfigurable FSSs [13]. Various designs of tunable FSSs have been proposed so far. In [14] and [15], tunable FSSs were achieved by mechanical deformation of the structure. In [16], another tunable FSS was developed by using a magnetically tunable ferrite substrate.

Although mechanical and magnetic tuning methods are low loss and require no bias network, they suffer from slow tuning speeds and small tuning ranges. Recently, a class of tunable FSS structures was designed based on liquid crystals [17]–[20]. Applying bias voltage to the liquid crystal changes its molecule orientation that in turn causes a change in the dielectric constant and the FSS frequency responses. However, the tuning ranges of the liquid-crystal-based structures are relatively limited. High-order tunable frequency-selective and phase-shifting surfaces were designed by integrating channels loaded with liquid metal droplets [21], [22]. By moving these droplets between the unit cells, the frequency response can be tuned continuously. Despite a higher order frequency response and a linear tuning without bias network, this method requires complicated and costly fabrication. Another approach to the reconfigurability was achieved by utilizing micro-electromechanical (MEMS) switches or capacitors to alter the unit cells [23]–[25]. Likewise, this approach demands complicated fabrication methods.

A well-known method for tuning microwave devices is to use active components such as varactors and PIN diodes [26]–[36]. They provide high-speed and wideband tuning with compact size and low cost [26]. However, one challenge in designing FSSs with these components is the need for bias network and the strategies that should be considered for RF/DC isolation. Adding the bias network and isolating elements affects the original frequency response of the FSS [13]. This issue is accentuated in developing FSSs with higher order filtering responses. Thus, so far, varactor-tunable high-order FSS has yet to be realized.

In this paper, a second-order bandpass FSS is proposed based on miniaturized elements with varactor-based tuning capability. The designed FSS is composed of three metallic layers separated from each other by thin dielectric spacers. The bias network is embedded in the FSS structure that comprises wire grids in all layers and vias that connect the varactors in the front and back layers to the middle layer. This configuration enables tunability without the need for any additional circuit or network for biasing the individual varactors. Since all the varactors are biased in parallel, only a single RF choke is needed for RF/DC isolation. Furthermore, miniaturized nonresonant or hybrid (combination of resonant and nonresonant) elements offer low-profile configurations with stable frequency responses with respect to the incidence angle of the electromagnetic wave [37]–[40].
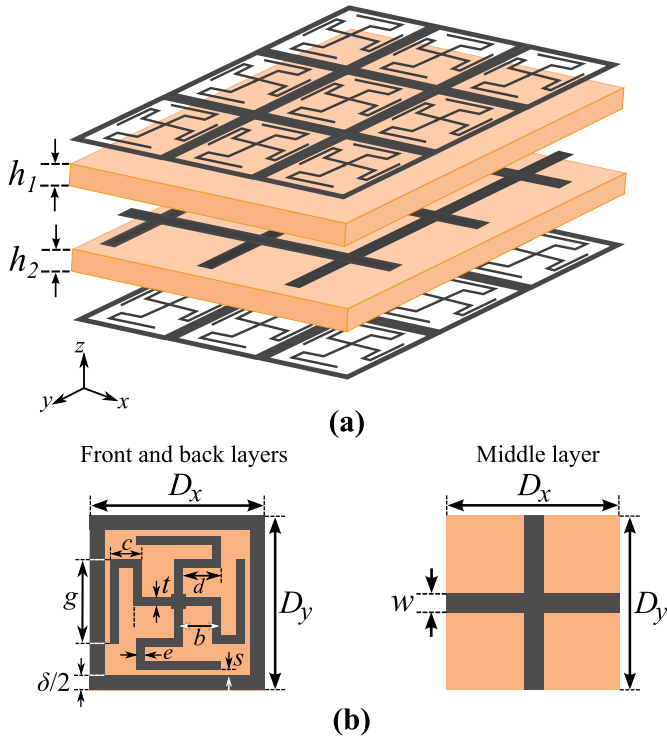
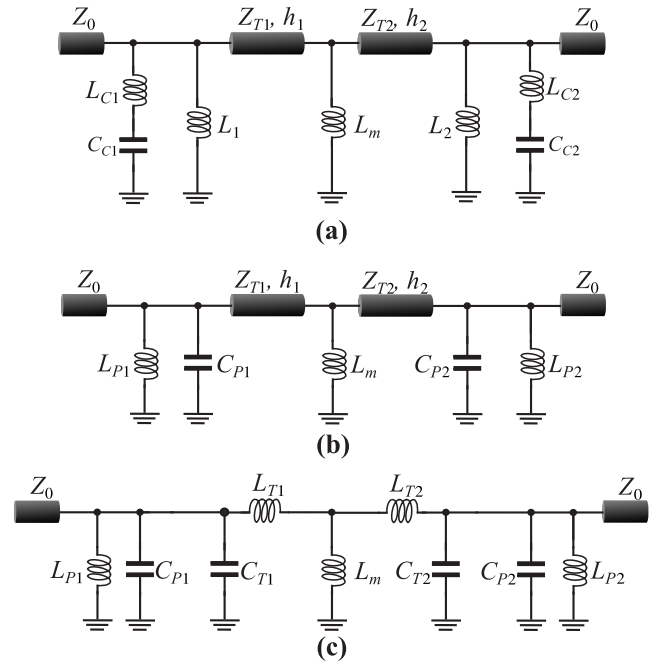Fig. 1. Structure of the proposed FSS. (a) 3-D exploded view of the FSS. (b) 2-D view of the unit cell.

Fig. 2. (a) Equivalent lumped-element circuit model of the proposed FSS. (b) Simplified circuit with the hybrid resonators replaced by their parallel LC equivalences. (c) Circuit with the transmission lines replaced with equivalent lumped elements models.

In the following, we first present the FSS structure and its equivalent circuit model in Section II. In Section III, a synthesis procedure is developed for this FSS based on the equivalent circuit model followed by an explanation of the tuning mechanism. Section IV presents the realization of the tunable FSS based on the method described in Section III. The proposed tunable FSS concept is experimentally verified in Section V. Finally, the conclusion is presented in Section VI.

II. FSS STRUCTURE AND EQUIVALENT CIRCUIT MODEL

A three-dimensional (3-D) view of the proposed FSS and the unit cells are demonstrated in Fig. 1. The structure is composed of three metallic layers that are separated from each other by two thin dielectric spacers. The top and bottom metallic layers consist of miniaturized meandered cross-shaped resonators surrounded by the inductive wire grid. The middle layer is made of another inductive wire grids. In the ideal form, the top and bottom metallic layers are exactly the same and the whole structure is symmetric with respect to the middle layer. The crossing points of the wire strips in middle layer are aligned with the center of the resonators on the front and back layers. The overall thickness of the structure is $2h$, where h is the thickness of each dielectric spacer. The dimensions of the unit cell along the x and y directions are specified by $D_x = D_y = D$.

Since the FSS is based on subwavelength unit cells, its electromagnetic response can be modeled through an equivalent lumped-element circuit model. The circuit model provides more insight into the FSS behavior. In addition, it can be used to synthesize an FSS from a desired filter response. The FSS circuit model under a normally incident plane wave is presented

in Fig. 2(a), where the front and back layers of the FSS are modeled by the series $L_C C_C$ resonators in parallel with L inductor, where 1 and 2 denote the front and back layers, respectively. The inductor L models the inductive effect of the wire grid. The series $L_C C_C$ resonators model the cross-shaped resonators, where L_C is the equivalent inductance of the resonator arms and C_C stands for the capacitive effect between the edges of the wire grid and the resonator arms in each unit. The middle layer wire grid is modeled with the parallel inductor L_m. Furthermore, the two dielectric spacers are modeled by the transmission line sections of length h with characteristic impedance of $Z_T = Z_0/\sqrt{\epsilon_r}$, where $Z_0 = 377\ \Omega$ is the free-space characteristic impedance and ϵ_r is the relative permittivity of the dielectric material. The free-space on the two sides of the FSS is modeled with transmission lines having a characteristic impedance $Z_0 = 377\ \Omega$. The equivalent circuit in Fig. 2(a) can be simplified to the one in Fig. 2(b) by replacing the front and back hybrid resonators with their parallel LC equivalence. The relations between the hybrid resonator and the parallel LC resonator are as follows [41], [42]: First, the frequency at which the equivalent admittance is nulled should be the same between the hybrid resonators in Fig. 2(a) and the parallel LC resonators in Fig. 2(b). This means

$$\frac{1}{\sqrt{(L + L_C)C_C}} = \frac{1}{\sqrt{L_P C_P}}. \qquad (1)$$

Second, the susceptance slope of the two resonators should be equal to each other at the center frequency of the filter. This condition leads to

$$C_C \left(\frac{L + L_C}{L}\right)^2 = C_P. \qquad (2)$$

The third condition for determining the hybrid resonator element values univocally is obtained by considering the transmission zero frequency provided by the series $L_C C_C$ branch in the hybrid resonator in Fig. 2(a). The transmission zero will improve the out-of-band rejection of the filter. The frequency of the transmission zero is given by

$$f_z = \frac{1}{2\pi\sqrt{L_C C_C}}. \tag{3}$$

A choice of the transmission zero is arbitrary. In this case, it is positioned close to the passband to improve the sharpness of the filter response in the upper rejection band.

III. FSS DESIGN

A. Synthesis Procedure of the FSS

By using the telegrapher's equation [43], subwavelength transmission line sections can be presented by their equivalent circuit models with series inductance $L_T = \mu_0\mu_r h$ and shunt capacitance $C_T = \epsilon_0\epsilon_r h/2$ where h is the spacer thickness, and μ_r and ϵ_r are the permeability and permittivity of the dielectric spacer, respectively. So, the circuit in Fig. 2(b) can be redrawn as the one in Fig. 2(c) that is a second-order coupled-resonator bandpass filter. Based on the circuit in Fig. 2(c), a synthesis procedure can be developed for the proposed FSS by applying the concept of coupled-resonator filter with inductive coupling [44], [45]. By specifying the center frequency of the FSS f_0 and the fractional bandwidth $\delta = \text{BW}/f_0$ to realize a desired filter type, e.g., Chebyshev, Butterworth, the element values can be designed for the circuit in Fig. 2(c). The design procedure can be summarized as follows.

1) The summation of the C_P and C_T capacitors for each of the front and back layers can be calculated by using the following equation:

$$C_i = C_{Pi} + C_{Ti} = \frac{q_i}{\omega_0 r_i Z_0 \delta}, \quad i = 1, 2 \tag{4}$$

where q_1 and q_2 are the normalized quality factors of the front and back layers resonators, respectively, $Z_0 = 377\ \Omega$ and r_1 and r_2 are the normalized source and load impedances for the circuit in Fig. 2(c).

2) The inductances L_{P1} and L_{P2} can be calculated as follows:

$$L_{Pi} = \frac{1}{\omega_0^2(C_i - k_{12}\delta\sqrt{C_1 C_2})}, \quad i = 1, 2 \tag{5}$$

where k_{12} is the normalized coupling coefficient between the input and output resonators in Fig. 2(c).

3) The middle layer inductance L_m is determined as

$$L_m = \frac{Z_0}{\omega_0 k_{12}} \cdot \frac{(k_{12}\delta)^2}{1 - (k_{12}\delta)^2} \cdot \sqrt{\frac{r_1 r_2}{q_1 q_2}}. \tag{6}$$

4) The equivalent inductances of the transmission line sections can be obtained as follows:

$$L_{T1} = \frac{\sqrt{L_m^2(1+\alpha)^2 + 4\alpha L_m L_{12}} - L_m(1+\alpha)}{2\alpha} \tag{7}$$

$$L_{T2} = \alpha L_{T1} \tag{8}$$

$$L_{12} = \frac{1}{\omega_0^2(k_{12}\delta\sqrt{C_1 C_2})} \tag{9}$$

$$\alpha = \frac{q_1}{q_2} \cdot \frac{1 - k_{12}\delta\sqrt{\dfrac{q_2 r_1}{q_1 r_2}}}{1 - k_{12}\delta\sqrt{\dfrac{q_1 r_2}{q_2 r_1}}}. \tag{10}$$

The normalized quality factors q_1, q_2 and coupling coefficients k_{12} for the second-order filter of different types can be extracted from the design tables in [44] and [45]. As mentioned before, the circuit in Fig. 2(c) is obtained from the one in Fig. 2(b) by using the telegrapher's equation. So, the lengths of the transmission line sections representing the dielectric spacers thickness in Fig. 2 can be calculated as

$$h_i = \frac{L_{Ti}}{\mu_0\mu_{ri}}, \quad i = 1, 2. \tag{11}$$

The values of the parallel capacitances C_{P1} and C_{P2} can then be obtained from

$$C_{Pi} = C_i - \frac{\epsilon_0\epsilon_{ri}h_i}{2}, \quad i = 1, 2. \tag{12}$$

Now, the element values of the front and back resonators in Fig. 2 can be determined by using (1)–(3).

The parameters of the equivalent circuit in Fig. 2(a) can be mapped to the geometrical dimensions of the FSS by using the method explained in [46]–[48]. It should be noted that the substrate thicknesses calculated from (11) might not be commercially available. These calculated geometrical values are treated as an initial approximation in the optimization procedure of the FSS using full-wave EM simulations. The effective inductance of a wire grid can be related to wire width w and the unit cell size D by using [1], [49]

$$L = \mu_0\mu_{\text{eff}} \frac{D}{2\pi} \ln\left(\frac{1}{\sin\frac{\pi w}{2D}}\right) \tag{13}$$

where μ_{eff} is the effective permeability of the substrate. Therefore, this equation can be used to design the middle-layer wire grid dimensions. To this end, the unit cell size D can be chosen arbitrarily, but it should be considered that a very small unit cell size leads to very thin wires that might not be implementable due to fabrication limits. The next step is to design the front and back hybrid resonators in a way that they satisfy the designed equivalent circuit elements, ($L_{1,2}$ and $L_C C_C$). Equation (13) also provides an approximation to the dimensions of the front and back wire grids. These wire grids are strongly influenced by the cross-shaped resonators, and thus require optimization to account for parasitic effects. As an initial step, the unit cell size of the hybrid resonator is set to equal the size of the middle wire grid D, and the width of the wire grid can be calculated from (13) to satisfy the required $L_{1,2}$. Next, the dimensions of the cross-shaped resonator are designed to match the required L_C and C_C. Specifically, the inductance L_C mainly depends on the width t and the length ($b + c + g$) of the resonator arms, while the capacitance C_C depends on the resonator arm length g and the gap between the arm and wire grid s. A realizable value can be chosen for the gap s. The length of
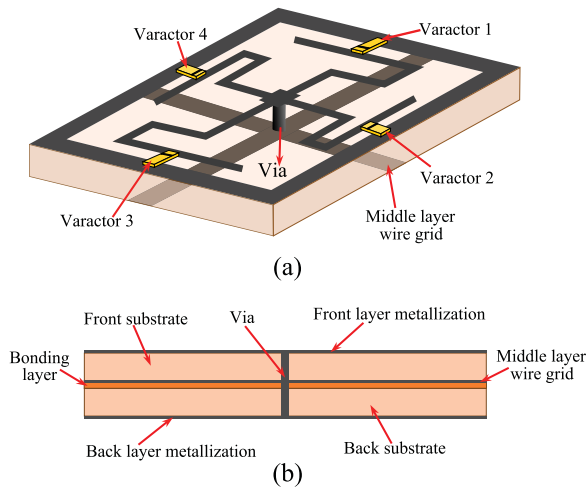
(a)

(b)

Fig. 3. (a) 3-D view of the front and middle layers of the unit cell. A metallic via and four varactor diodes are included in each unit cell for tuning. The back layer and the other dielectric spacers are not drawn for clarity. The black strips show the cathode side of the varactors. (b) Cross-sectional view of the unit cell indicating the three metallizations, vias and the bonding layer.

the cross-shaped resonator arms $2(b + c + g)$ is initially chosen to be half of the wavelength at the transmission zero frequency f_z. From these initial geometrical values of the resonator, the associated L_C and C_C values can be confirmed by a semiana-lytical procedure as follows. In the EM simulation, f_z for this initial design can be determined. Then by adding an arbitrary lumped capacitor of C_{ar} between the resonator arms and the wire grid, the transmission-zero frequency will be red-shifted to

$$f_{z1} = \frac{1}{2\pi\sqrt{L_C(C_C + C_{ar})}}. \quad (14)$$

Thus, by solving (3) and (14), the values of L_C and C_C can be calculated. If the obtained L_C and C_C match the designed parameters from the circuit synthesis, the optimization is finished for the cross-shaped resonator. Otherwise, the procedure is repeated until the results converge. After optimizing the cross-shaped resonators, the width of the wire grid δ can be optimized by curve fitting the EM and circuit simulation results around the null frequency of the hybrid resonator that is described by (1). After obtaining the optimized δ, the transmission zero frequency f_z might be slightly shifted. This shift can be compensated by a slight adjustment of the cross-shaped resonator arm $(b + c + g)$ and t.

B. Tuning Mechanism

The proposed FSS can be simply modified to exhibit a tunable response by loading varactors in the front and back layers, as shown in Fig. 3(a) (with the back layer excluded for clarity). A metallic via in each unit cell is used to electrically connect the front and back cross-shaped resonator to the middle layer wire grid. This configuration is elaborated in Fig. 3(b) through the cross-sectional view of the unit cell. The varactors are loaded in the gaps between the cross-shaped resonator arms and the front and back wire grids. By applying a DC bias voltage between the middle wire grid and the front and back wire grids, the equivalent capacitance (C_{C1} and C_{C2}) between the

cross-shaped resonators and the wire grids in front and back layers can be varied resulting in a tunable frequency response for the FSS. In this condition, the equivalent capacitances of the hybrid resonators can be defined as a summation of the varactor capacitance C_{var} and the capacitance between the cross-shaped resonators and wire grids C_0

$$C_{Ci} = C_{var} + C_{0i}, \; i = 1, 2. \quad (15)$$

A significant benefit of this structure compared with other varactor-tunable FSSs [26]–[28] is that in this case, all the varactors are electrically biased in parallel and no additional bias networks such as thin bias wires, resistors, or lumped capacitors are needed. It requires only a single RF choke to connect in series with the DC voltage supply to isolate dc circuitry from RF.

IV. STRUCTURE REALIZATION

The synthesis procedure described in Section III has been used to design a varactor-loaded FSS having a center frequency of 5.2 GHz and a fractional bandwidth of $\delta = 9\%$. The loaded varactor is with minimum capacitance of 0.12 pF. A transmission zero is positioned at $f_z = 6$ GHz to improve the upper band selectivity of the filter. The FSS is designed to exhibit a Butterworth response, and so the extracted k_{12} and q values are 1.4142 and 0.707, respectively. The Teconic TLY-5 with a relative permittivity of 2.2 and a loss tangent of 0.0009 is chosen as the dielectric substrate. Based on this specification and from (1) to (10), the equivalent circuit parameters are calculated as: $L_m = 4.5$ nH, $C_{C1} = C_{C2} = 0.21$ pF, $L_{C1} = L_{C2} = 2.78$ nH, $L_1 = L_2 = 1.7$ nH. The calculated spacers thickness $h_1 = h_2 = 1.65$ mm is not commercially available. Therefore, we have chosen $h = 1.52$ mm that is the closest commercially available thickness. Furthermore, the front and back dielectric spacers have to be bonded to each other. The bonding layer consists of a 0.1-mm-thick Rogers 4450F with a relative permittivity of $\epsilon_r = 3.58$. The cross-sectional view of the FSS unit cell in presented in Fig. 3(b) for clarity. The presence of this thin bonding layer introduces asymmetry, which can be compensated via optimization. The optimization is carried out at the circuit level in advanced design system (ADS). In the simulation, this bonding layer is represented by a transmission line with a length of 0.1 mm and a characteristic impedance of $207.5\,\Omega$ in series with the transmission line that represents the back spacer. The h values are kept constant, whereas the other circuit parameters are tuned to achieve the specified filter characteristics. It should be mentioned that in the optimization, the circuit parameters obtained from (1) to (10) are considered as initial values. Having these initial values significantly simplifies the optimization process.

In the next step, the optimized circuit parameters in ADS are converted to the physical dimensions of the FSS by using a procedure explained in Section III. In full-wave simulations, four lumped capacitors each with 0.12 pF are placed between the cross-shaped resonator arms and wire grids in each of the front and back layers of the FSS to model the varactor diodes. The varactor diode is MA46H120 from M/A-COM which is a GaAs flip-chip diode and provides a range of capacitance
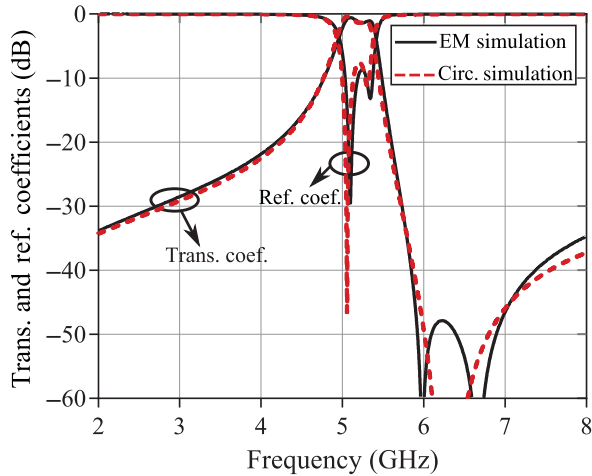
Fig. 4. Comparison between the circuit model and full-wave electromagnetic simulation results of the designed FSS. The optimized equivalent circuit parameters are: $C_{C1} = 0.251$ pF, $C_{C2} = 0.231$ pF $L_{C1} = 2.48$ nH, $L_{C2} = 2.65$ nH, $L_1 = 1.95$ nH, $L_2 = 2.07$ nH, $L_m = 3.1$ nH. The unit cell geometrical dimensions are: $h_1 = h_2 = 1.52$ mm, $D_x = D_y = 8$ mm, $\delta_1 = \delta_2 = 0.9$ mm, $g_1 = 3.8$ mm, $t_1 = t_2 = e_1 = 0.6$ mm, $e_2 = 0.3$ mm, $s_1 = s_2 = 0.3$ mm, $b_1 = b_2 = 2.3$ mm, $c_1 = c_1 = 1.25$ mm, $d_1 = 1.6$ mm, $d_2 = 1.5$ mm, and $w = 0.65$ mm.

between 0.12 and 1.00 pF for a reverse bias voltage between 16 and 0 V. The optimized equivalent circuit and the geometrical parameters of the designed FSS are listed in the caption of Fig. 4. The slight difference in the dimensions and circuit parameters between the front and back layers reflect the asymmetry that is imposed by the bonding layer. The simulated fractional bandwidth is 8.8% and the upper stopband transmission zero is achieved at 5.97 GHz, close to the desired filter specifications. A comparison in Fig. 4 shows a good agreement between the circuit model and 3-D EM simulation results.

V. RESULTS AND DISCUSSIONS

A prototype of the designed FSS in Section IV has been fabricated and tested inside a parallel-plate waveguide to show the validity of the design and the effectiveness of the tuning method. The parallel-plate waveguide setup is used since it supports a TEM wave propagation, which is the same a free-space plane-wave excitation. An array of 3×18 unit cells is fabricated to match the dimensions of the waveguide aperture. The overall thickness of the fabricated sample is 3.14 mm, which is less than $\lambda_0/18$ at 5.2 GHz. The cross-shaped resonators in the front and back layers of the FSS are connected to the middle-layer wire grid through vias with 0.3 mm diameter. A 47-kΩ resistor is soldered to the middle-layer wire grid to act as an RF choke. The fabricated prototype and its front and back unit cells are demonstrated in Fig. 5. Since the TEM mode can be excited inside the parallel-plate waveguide in the frequency range of interest [50]–[52], only two varactors aligned with the E-field direction are soldered in each side of the unit cell. The parallel plate waveguide test setup is depicted in Fig. 6. The FSS is then placed inside the waveguide and the bias wires are connected to a variable DC power supply. In this way, all the varactors are reverse-biased and by changing the dc bias voltage (V_b), the varactors' capacitance will be tuned.
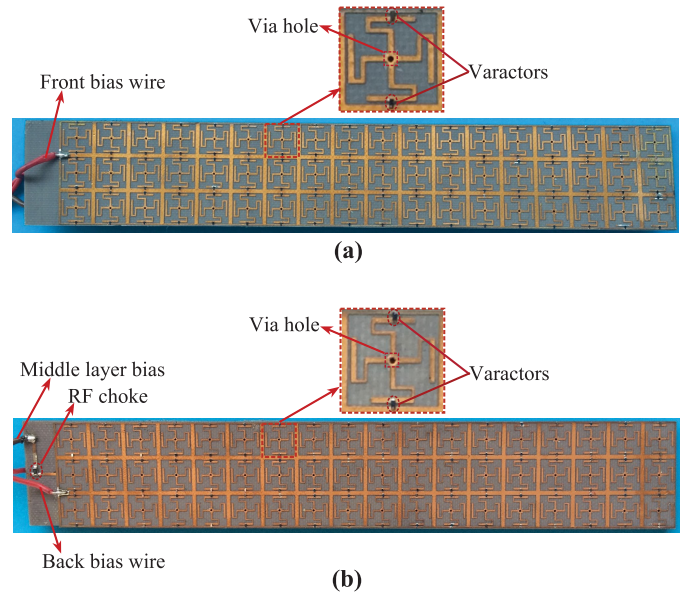

(a)

(b)

Fig. 5. Fabricated FSS prototype. (a) Front layer with an inset showing a unit cell. (b) Back layer with an inset showing a unit cell. A red wire is soldered to the front and back wire grids to apply the negative bias voltage. A black wire in series with the RF choke is soldered to the middle wire grid to provide the grounding.
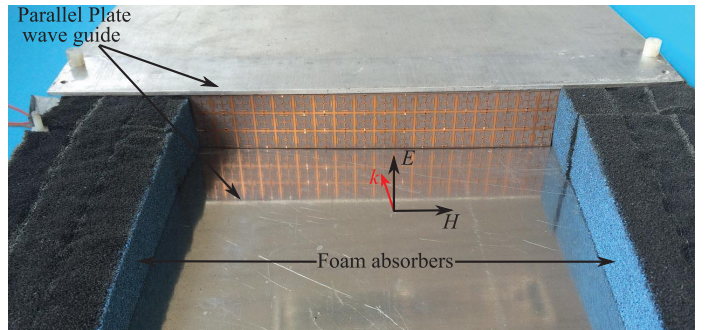

Fig. 6. FSS inside the parallel-plate waveguide testing platform.

In the measurements, first the bias voltage is set to 16 V to yield the lowest capacitor value of 0.12 pF for each varactor, which corresponds to a center frequency of 5.2 GHz for the filter response. Then, the bias voltage is decreased step by step and the corresponding transmission response has been recorded for each step. The normalized measured transmission responses of the FSS for different bias voltages are plotted in Fig. 7 together with the results from EM simulations for normal incidence. The EM simulations in CST Microwave Studio are carried out with the Floquet boundary condition to replicate an infinite planar array of the unit cells.

There is a good agreement between the simulated and the measured results. The discrepancies between them are mostly attributed to the small air gap between the top and bottom plates of the waveguide and the FSS edges that would be improved if free-space measurement setup is used. The passband is defined at -3 dB from the peak of the transmission response. The maximum measured insertion loss within the FSS passband varies from 3 dB to around 6 dB when the reverse bias voltage varies from 16 to 4 V, respectively. This is mostly caused by the
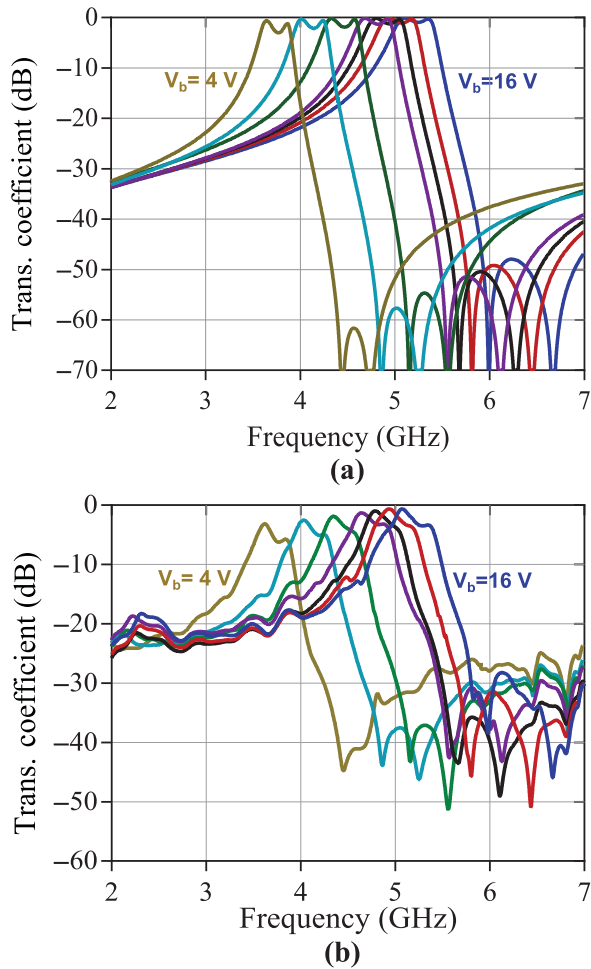
Fig. 7. Transmission responses of the designed tunable FSS under normal incidence for different values of varactor bias voltage. The reverse bias voltage (V_b) is varied from 16 to 4 V with a step size of 2 V. (a) Results obtained from EM simulations. (b) Measured transmission responses.
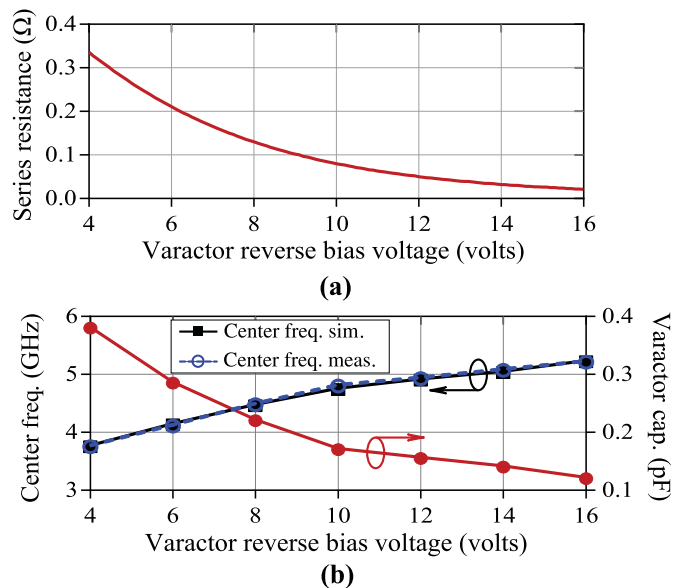

Fig. 8. (a) Series resistance of the varactor as a function of the bias voltage. (b) Variation in the varactor diode capacitance and the center frequency of the FSS as a function of the reverse bias voltage.
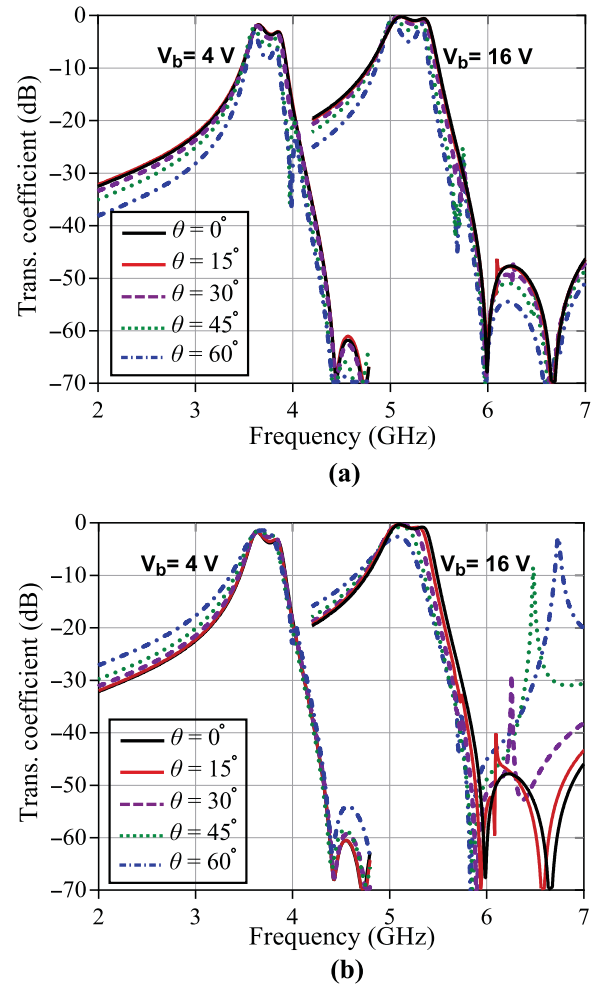

Fig. 9. Simulated transmission responses of the tunable FSS for oblique incidence angles (a) TE polarization and (b) TM polarization.

ohmic loss in the varactor diodes. The insertion loss increases when the bias voltage is decreased because the varactor exhibits a larger series resistance at lower bias voltage. Fig. 8(a) plots the characteristics of the series parasitic resistance of the varactor as function of the reverse bias voltage obtained from the manufacturer's SPICE model [53], [54]. The FSS center frequency and the varactor capacitance versus the bias voltage are plotted in Fig. 8(b). As seen, the simulated and measured center frequencies are very close to each other. The variation in the center frequency is smoother for the voltages above 10 V, and it becomes sharper for the smaller voltages. This is due to the nonlinear relationship between the varactor capacitance and the bias voltage, where below 10 V, the slope of the capacitance is larger than the slope for higher bias voltages.

The sensitivity of the FSS transmission response to the oblique incidences is examined by using 3-D EM simulations for both the TE and TM polarizations of the incident wave. The results are demonstrated in Fig. 9 for both the upper and lower limits of the tuning band. It is observed that the designed FSS shows a stable passband frequency response over a wide range of the incident angles up to $60°$ for both polarizations. This stability is a result of the very thin profile and the miniaturized dimensions of the unit cells [49]. However, weak resonances

appear in the out-of-band response for oblique incidences, and sharp harmonics appear in the upper stopband for the TM responses. The weak resonances are mainly attributed to the field imbalance across the FSS unit cells that excites higher order resonance modes. The out-of-band sharp harmonics in the TM responses are because of the longitudinal component of the electric field that couples with the conductive vias. This effect can be modeled by adding an inductance between the middle layer and series $L_C C_C$ resonators. These out-of-band resonances can be suppressed by fabricating vias with a smaller diameter.

VI. CONCLUSION

A second-order tunable frequency-selective surface has been designed for microwave applications. A design procedure based on a circuit model has been developed for synthesizing the FSS using the standard filter theory. The tunability is achieved by integrating varactor diodes in the front and back layers. A unique feature of the structure is that all the varactors are biased in parallel via the FSS structure without a dedicated bias network. The proposed tunable FSS concept has been verified by measuring a fabricated prototype in a parallel-plate waveguide. The measurement results show a continuous tuning range from 5.2 to 3.7 GHz for the center frequency. In addition, the simulations show consistent frequency responses for the FSS under a wide range of oblique incidence angles for both the TE and TM polarizations.

REFERENCES

[1] B. A. Munk, *Frequency Selective Surfaces: Theory and Design*. Hoboken, NJ, USA: Wiley, 2005.

[2] A. Ebrahimi, W. Withayachumnankul, S. Al-Sarawi, and D. Abbott, "Design of dual-band frequency selective surface with miniaturized elements," in *Proc. Int. Workshop Antenna Technol.: "Small Antennas, Novel EM Struct. Mater. Appl." (iWAT)*, Mar. 2014, pp. 201–204.

[3] A. Ebrahimi, W. Withayachumnankul, S. Al-Sarawi, and D. Abbott, "Second-order bandpass frequency selective surface for terahertz applications," in *Proc. 39th Int. Conf. Infrared Millimeter Terahertz Waves (IRMMW-THz)*, Sep. 2014, doi: 10.1109/IRMMW-THz.2014.6956237.

[4] B. Li and Z. Shen, "Synthesis of quasi-elliptic bandpass frequency-selective surface using cascaded loop arrays," *IEEE Trans. Antennas Propag.*, vol. 61, no. 6, pp. 3053–3059, Jun. 2013.

[5] S. Momeni Hasan Abadi, M. Li, and N. Behdad, "Harmonic-suppressed miniaturized-element frequency selective surfaces with higher order bandpass responses," *IEEE Trans. Antennas Propag.*, vol. 62, no. 5, pp. 2562–2571, May 2014.

[6] B. Chambers and K. Ford, "Tunable radar absorbers using frequency selective surfaces," in *Proc. IEE 11th Int. Conf. Antennas Propag.*, 2001, vol. 2, pp. 593–597.

[7] K. Ford and B. Chambers, "Smart microwave absorber," *Electron. Lett.*, vol. 36, no. 1, pp. 50–52, Jan. 2000.

[8] J. Yang and Z. Shen, "A thin and broadband absorber using double-square loops," *IEEE Antennas Wireless Propag. Lett.*, vol. 6, pp. 388–391, Dec. 2007.

[9] M. Euler and V. Fusco, "Frequency selective surface using nested split ring slot elements as a lens with mechanically reconfigurable beam steering capability," *IEEE Trans. Antennas Propag.*, vol. 58, no. 10, pp. 3417–3421, Oct. 2010.

[10] M. Li, M. Al-Joumayly, and N. Behdad, "Broadband true-time-delay microwave lenses based on miniaturized element frequency selective surfaces," *IEEE Trans. Antennas Propag.*, vol. 61, no. 3, pp. 1166–1179, Mar. 2013.

[11] S. Hasan Abadi, K. Ghaemi, and N. Behdad, "Ultra-wideband, true-time-delay reflectarray antennas using ground-plane-backed, miniaturized-element frequency selective surfaces," *IEEE Trans. Antennas Propag.*, vol. 63, no. 2, pp. 534–542, Feb. 2015.

[12] T. Niu *et al.*, "Terahertz reflectarray as a polarizing beam splitter," *Opt. Exp.*, vol. 22, no. 13, pp. 16 148–16 160, 2014.

[13] F. Bayatpur and K. Sarabandi, "Design and analysis of a tunable miniaturized-element frequency-selective surface without bias network," *IEEE Trans. Antennas Propag.*, vol. 58, no. 4, pp. 1214–1219, Apr. 2010.

[14] S. Azemi, K. Ghorbani, and W. Rowe, "A reconfigurable FSS using a spring resonator element," *IEEE Antennas Wireless Propag. Lett.*, vol. 12, pp. 781–784, Jul. 2013.

[15] K. Fuchi, J. Tang, B. Crowgey, A. Diaz, E. Rothwell, and R. Ouedraogo, "Origami tunable frequency selective surfaces," *IEEE Antennas Wireless Propag. Lett.*, vol. 11, pp. 473–475, May 2012.

[16] T. Chang, R. Langley, and E. Parker, "Frequency selective surfaces on biased ferrite substrates," *Electron. Lett.*, vol. 30, no. 15, pp. 1193–1194, Jul. 1994.

[17] A. Ebrahimi, P. Yaghmaee, W. Withayachumnankul, C. Fumeaux, S. Al-Sarawi, and D. Abbott, "Interlayer tuning of X-band frequency-selective surface using liquid crystal," in *Proc. Asia-Pac. Microw. Conf. (APMC)*, Nov. 2013, pp. 1118–1120.

[18] J. Bossard *et al.*, "Tunable frequency selective surfaces and negative-zero-positive index metamaterials based on liquid crystals," *IEEE Trans. Antennas Propag.*, vol. 56, no. 5, pp. 1308–1320, May 2008.

[19] W. Hu *et al.*, "Liquid crystal tunable MM-wave frequency selective surface," *IEEE Microw. Wireless Compon. Lett.*, vol. 17, no. 9, pp. 667–669, Sep. 2007.

[20] P. Yaghmaee, W. Withayachumnankul, A. Horestani, A. Ebrahimi, B. Bates, and C. Fumeaux, "Tunable electric-LC resonators using liquid crystal," in *Proc. Antennas Propag. Soc. Int. Symp. (APSURSI)*, Jul. 2013, pp. 382–383.

[21] M. Li and N. Behdad, "Fluidically tunable frequency selective/phase shifting surfaces for high-power microwave applications," *IEEE Trans. Antennas Propag.*, vol. 60, no. 6, pp. 2748–2759, Jun. 2012.

[22] M. Li, B. Yu, and N. Behdad, "Liquid-tunable frequency selective surfaces," *IEEE Microw. Wireless Compon. Lett.*, vol. 20, no. 8, pp. 423–425, Aug. 2010.

[23] G. Coutts, R. Mansour, and S. Chaudhuri, "Microelectromechanical systems tunable frequency-selective surfaces and electromagnetic-bandgap structures on rigid-flex substrates," *IEEE Trans. Microw. Theory Techn.*, vol. 56, no. 7, pp. 1737–1746, Jul. 2008.

[24] B. Schoenlinner, A. Abbaspour-Tamijani, L. C. Kempel, and G. Rebeiz, "Switchable low-loss RF MEMS Ka-band frequency-selective surface," *IEEE Trans. Microw. Theory Techn.*, vol. 52, no. 11, pp. 2474–2481, Nov. 2004.

[25] J. Zendejas, J. Gianvittorio, Y. Rahmat-Samii, and J. Judy, "Magnetic MEMS reconfigurable frequency-selective surfaces," *J. Microelectromech. Syst.*, vol. 15, no. 3, pp. 613–623, Jun. 2006.

[26] X. Huang, Z. Shen, Q. Feng, and B. Li, "Tunable 3-D bandpass frequency-selective structure with wide tuning range," *IEEE Trans. Antennas Propag.*, vol. 63, no. 7, pp. 3297–3301, Jul. 2015.

[27] C. Mias, "Varactor-tunable frequency selective surface with resistive-lumped-element biasing grids," *IEEE Microw. Wireless Compon. Lett.*, vol. 15, no. 9, pp. 570–572, Sep. 2005.

[28] W. Pan, C. Huang, P. Chen, X. Ma, and X. Luo, "A beam steering horn antenna using active frequency selective surface," *IEEE Trans. Antennas Propag.*, vol. 61, no. 12, pp. 6218–6223, Dec. 2013.

[29] F. Bayatpur and K. Sarabandi, "A tunable metamaterial frequency-selective surface with variable modes of operation," *IEEE Trans. Microw. Theory Techn.*, vol. 57, no. 6, pp. 1433–1438, Jun. 2009.

[30] F. Costa, A. Monorchio, and G. Vastante, "Tunable high-impedance surface with a reduced number of varactors," *IEEE Antennas Wireless Propag. Lett.*, vol. 10, pp. 11–13, Mar. 2011.

[31] C. Mias, "Varactor tunable frequency selective absorber," *Electron. Lett.*, vol. 39, no. 14, pp. 1060–1062, Jul. 2003.

[32] G. Kiani, K. Ford, L. Olsson, K. Esselle, and C. Panagamuwa, "Switchable frequency selective surface for reconfigurable electromagnetic architecture of buildings," *IEEE Trans. Antennas Propag.*, vol. 58, no. 2, pp. 581–584, Feb. 2010.

[33] W. Withayachumnankul, C. Fumeaux, and D. Abbott, "Planar array of electric-LC resonators with broadband tunability," *IEEE Antennas Wireless Propag. Lett.*, vol. 10, pp. 577–580, Jun. 2011.

[34] G. I. Kiani, K. L. Ford, K. P. Esselle, A. R. Weily, C. Panagamuwa, and J. C. Batchelor, "Single-layer bandpass active frequency selective surface," *Microw. Opt. Technol. Lett.*, vol. 50, no. 8, pp. 2149–2151, 2008.

[35] A. Ebrahimi, W. Withayachumnankul, S. Al-Sarawi, and D. Abbott, "Higher-order tunable frequency selective surface with miniaturized elements," in *Proc. Mediterr. Microw. Symp.*, Dec. 2015, pp. 140–143.

[36] M. Sazegar *et al.*, "Beam steering transmitarray using tunable frequency selective surface with integrated ferroelectric varactors," *IEEE Trans. Antennas Propag.*, vol. 60, no. 12, pp. 5690–5699, Dec. 2012.

[37] A. Ebrahimi *et al.*, "Second-order terahertz bandpass frequency selective surface with miniaturized elements," *IEEE Trans. Terahertz Sci. Technol.*, vol. 5, no. 5, pp. 761–769, Sep. 2015.

[38] F. Bayatpur and K. Sarabandi, "Single-layer high-order miniaturized-element frequency-selective surfaces," *IEEE Trans. Microw. Theory Techn.*, vol. 56, no. 4, pp. 774–781, Apr. 2008.

[39] M. Kashanianfard and K. Sarabandi, "Metamaterial inspired optically transparent band-selective ground planes for antenna applications," *IEEE Trans. Antennas Propag.*, vol. 61, no. 9, pp. 4624–4631, Sep. 2013.

[40] M. Al-Joumayly and N. Behdad, "Low-profile, highly-selective, dual-band frequency selective surfaces with closely spaced bands of operation," *IEEE Trans. Antennas Propag.*, vol. 58, no. 12, pp. 4042–4050, Dec. 2010.

[41] J. Bonache *et al.*, "Super compact (<1 cm^2) band pass filters with wide bandwidth and high selectivity at C-band," in *Proc. 36th Eur. Microw. Conf.*, Sep. 2006, pp. 599–602.

[42] J. Bonache, I. Gil, J. García-García, and F. Martín, "Compact microstrip band-pass filters based on semi-lumped resonators," *IET Microw. Antennas Propag.*, vol. 1, no. 4, pp. 932–936, Aug. 2007.

[43] D. M. Pozar, *Microwave Engineering*. Hoboken, NJ, USA: Wiley, 2009.

[44] A. I. Zverev, *Handbook of Filter Synthesis*. Hoboken, NJ, USA: Wiley, 1967, vol. 47.

[45] M. Al-Joumayly and N. Behdad, "A new technique for design of low-profile, second-order, bandpass frequency selective surfaces," *IEEE Trans. Antennas Propag.*, vol. 57, no. 2, pp. 452–459, Feb. 2009.

[46] N. Behdad, M. Al-Joumayly, and M. Salehi, "A low-profile third-order bandpass frequency selective surface," *IEEE Trans. Antennas Propag.*, vol. 57, no. 2, pp. 460–466, Feb. 2009.

[47] N. Behdad and M. Al-Joumayly, "A generalized synthesis procedure for low-profile, frequency selective surfaces with odd-order bandpass responses," *IEEE Trans. Antennas Propag.*, vol. 58, no. 7, pp. 2460–2464, Jul. 2010.

[48] M. Al-Joumayly and N. Behdad, "A generalized method for synthesizing low-profile, band-pass frequency selective surfaces with non-resonant constituting elements," *IEEE Trans. Antennas Propag.*, vol. 58, no. 12, pp. 4033–4041, Dec. 2010.

[49] F. Bayatpur, "Metamaterial-inspired frequency-selective surfaces," Ph.D. dissertation, Dept. Elect. Eng. Comput. Sci., Univ. Michigan, Ann Arbor, MI, USA, 2009.

[50] Y. Shang, Z. Shen, and S. Xiao, "On the design of single-layer circuit analog absorber using double-square-loop array," *IEEE Trans. Antennas Propag.*, vol. 61, no. 12, pp. 6022–6029, Dec. 2013.

[51] B. Li and Z. Shen, "Wideband 3D frequency selective rasorber," *IEEE Trans. Antennas Propag.*, vol. 62, no. 12, pp. 6536–6541, Dec. 2014.

[52] Y. Shang, Z. Shen, and S. Xiao, "Frequency-selective rasorber based on square-loop and cross-dipole arrays," *IEEE Trans. Antennas Propag.*, vol. 62, no. 11, pp. 5581–5589, Nov. 2014.

[53] N. Nguyen-Trong, T. Kaufmann, L. Hall, and C. Fumeaux, "Analysis and design of a reconfigurable antenna based on half-mode substrate-integrated cavity," *IEEE Trans. Antennas Propag.*, vol. 63, no. 8, pp. 3345–3352, Aug. 2015.

[54] MACOM Technology Solutions. (2016, Jan.). *MA46H120 Varactor Datasheet*, [Online]. Available: Available: http://cdn.macom.com/datasheets/MA46H120.pdf.

Amir Ebrahimi (S'09) received the B.Sc. degree in electrical engineering from the University of Mazandaran, Babol, Iran, in 2008, and the M.Sc. degree in electronic engineering from Babol University of Technology, Babol, Iran, in 2011. Currently, he is pursuing the Ph.D. degree in electrical and electronic engineering from the University of Adelaide, Adelaide, S.A., Australia.

From 2009 to 2012, he was a Research Assistant with the Integrated Circuits Research Laboratory (ICRL), Babol University of Technology. He was a Visiting Research Fellow at Nanyang Technological University (NTU), Singapore, during 2014–2015. His research interests include metamaterial-inspired microwave devices, microwave circuit design, microwave filters, frequency-selective surfaces (FSSs) and nonlinear RF, and microwave circuits design and analysis.

Mr. Ebrahimi was the recipient of the International Postgraduate Research (Ph.D.) Scholarship (IPRS) by the Australian Government in 2012, the Australian Postgraduate Award (APA) in 2012, the Australian National Fabrication Facility (ANFF) Award in 2013, the University of Adelaide D.R. Stranks Traveling Fellowship in 2014, the Simon Rockliff Scholarship presented by DSTG in 2015, the Yarman–Carlin Best Student Paper Award at the Mediterranean Microwave Symposium in 2015, and the Best Student Paper at the Australian Microwave Symposium in 2016.

Zhongxiang Shen (M'98–SM'04) received the B.Eng. degree from the University of Electronic Science and Technology of China, Chengdu, China, in 1987, the M.S. degree from Southeast University, Nanjing, China, in 1990, and the Ph.D. degree from the University of Waterloo, Waterloo, ON, Canada, in 1997, all in electrical engineering.

From 1990 to 1994, he was with Nanjing University of Aeronautics and Astronautics, Nanjing, China. He was with Com Dev Ltd., Cambridge, ON, Canada, as an Advanced Member of Technical Staff in 1997. He spent six months each in 1998, first with the Gordon McKay Laboratory, Harvard University, Cambridge, MA, USA, and then with the Radiation Laboratory, University of Michigan, Ann Arbor, MI, USA, as a Postdoctoral Fellow. In 1999, he joined Nanyang Technological University (NTU), Singapore, as an Assistant Professor. He has been an Associate Professor with the School of Electrical and Electronic Engineering, NTU, since January 2004. His research interests include design of small and planar antennas for various wireless communication systems, analysis and design of frequency-selective structures and absorbers, hybrid numerical techniques for modeling RF/microwave components and antennas.

Dr. Shen is a Member of the Antennas and Propagation and Microwave Theory and Techniques Societies of the IEEE. He served as Chair of the IEEE MTT/AP Singapore Chapter. He was the Chair of AP-S Chapter Activities Committee from January 2010 to August 2014. He is currently serving as the Secretary of IEEE AP-S. He has authored/coauthored more than 130 journal papers and presented another 120 conference papers.

Withawat Withayachumnankul received the B.Eng. and M.Eng. degrees in electronic engineering from King Mongkut's Institute of Technology Ladkrabang (KMITL), Bangkok, Thailand, in 2001 and 2003, respectively, and the Ph.D. degree in electrical engineering (with commendation) from the University of Adelaide, Adelaide, S.A., Australia, in 2010.

From 2003 to 2012, he served as a Lecturer with the Faculty of Engineering, KMITL. From 2010 to 2013, he has held an ARC Australian Postdoctoral Fellowship with the University of Adelaide. Since 2014, he has taken up a position as a Lecturer with the University of Adelaide. Currently, he is also a JSPS Visiting Fellow at Tokyo Institute of Technology, Japan, and an Associate of RMIT University, Melbourne, Vic., Australia. He has authored or coauthored more than 50 journal publications. His research interests include terahertz technology, metamaterials, plasmonics, and optical antennas.

Dr. Withayachumnankul has delivered invited talks at ETH Zürich (ETHZ), University of Marburg, Universität Kaiserslautern, EPFL, IPHT (Germany), The University of Western Australia, and Ibaraki University. He serves as a Grant Assessor for Swiss National Science Foundation (SNSF), German Academic Exchange Service (DAAD), and Australian Research Council (ARC). He was the recipient of the IEEE/LEOS Graduate Student Fellowship (2008) and the SPIE Scholarship in Optical Science and Engineering (2008).

Said Al-Sarawi (M'92) received the general certificate in marine radio communication and the B.Eng. degree (first class Hons.) in marine electronics and communication from the Arab Academy for Science and Technology (AAST), Alexandria, Egypt, in 1987 and 1990, respectively, and the Ph.D. degree in mixed analog and digital circuit design techniques for smart wireless systems, with special commendation in electrical and electronic engineering, from the University of Adelaide, Adelaide, S.A., Australia, in 2003.

Currently, he is the Director of the Centre for Biomedical Engineering and a Founding Member of Education Research Group of Adelaide (ERGA) at the University of Adelaide. His research interests include design techniques for mixed signal systems in CMOS and optoelectronic technologies for high-performance radio transceivers, low-power and low-voltage radio frequency identification (RFID) systems, data converters,

mixed-signal design, microelectromechanical systems (MEMS) for biomedical applications, innovative teaching techniques for engineering education, research skill development, and factors affecting students evaluations of courses in different disciplines.

Dr. Al-Sarawi was the recipient of the University of Adelaide Alumni Postgraduate Medal (formerly Culross Prize) for outstanding academic merit at the postgraduate level. While pursuing his Ph.D., he won the Commonwealth Postgraduate Research Award (Industry). He also received the Graduate Certificate in Education (Higher Education), in 2006, from the same university.

Derek Abbott (M'85–SM'99–F'05) was born in South Kensington, London, U.K., in 1960. He received the B.Sc. (Hons.) degree in physics from Loughborough University, Loughborough, U.K., in 1982, and the Ph.D. degree in electrical and electronic engineering from the University of Adelaide, Adelaide, S.A., Australia, in 1995, under K. Eshraghian and B. R. Davis.

From 1978 to 1986, he was a Research Engineer with the GEC Hirst Research Centre, London, U.K. From 1986 to 1987, he was a VLSI Design Engineer with Austek Microsystems, Australia. Since 1987, he has been with the University of Adelaide, where he is currently a Full Professor with the School of Electrical and Electronic Engineering. He coedited *Quantum Aspects of Life* (London, U.K.: Imperial College Press, 2008), coauthored *Stochastic Resonance* (Cambridge, U.K.: Cambridge University Press, 2012), and coauthored *Terahertz Imaging for Biomedical Applications* (New York, NY, USA: Springer-Verlag, 2012). He holds over 800 publications/patents and has been an invited speaker at over 100 institutions. His research interests include the area of multidisciplinary physics and electronic engineering applied to complex systems, areas of stochastics, game theory, photonics, biomedical engineering, and computational neuroscience.

Prof. Abbott is a Fellow of the Institute of Physics (IOP). He has served as an Editor and/or Guest Editor for a number of journals including *IEEE Journal of Solid-State Circuits*, *Journal of Optics B* (IOP), *Microelectronics Journal* (Elsevier), *Chaos* (AIP), *Smart Structures and Materials* (IOP), *Journal of Optics B* (IOP), *Fluctuation and Noise Letters*, *PLOSONE*, *Proceedings of the IEEE* and is now on on the editorial boards of *IEEE Access*, *Nature Scientific Reports*, *Royal Society Open Science*, and *Frontiers in Physics*. He was the recipient of the South Australian Tall Poppy Award for Science (2004), the Premier's SA Great Award in Science and Technology for outstanding contributions to South Australia (2004), the Australian Research Council (ARC) Future Fellowship (2012), and the David Dewhurst Medal (2015).